

# PathDiff: Histopathology Image Synthesis with Unpaired Text and Mask Conditions

Mahesh Bhosale<sup>1</sup>   Abdul Wasi<sup>1</sup>   Yuanhao Zhai<sup>1</sup>   Yunjie Tian<sup>1</sup>   Samuel Border<sup>2</sup>  
 Nan Xi<sup>1</sup>   Pinaki Sarder<sup>2</sup>   Junsong Yuan<sup>1</sup>   David Doermann<sup>1</sup>  
 Xuan Gong<sup>3</sup>

<sup>1</sup>University at Buffalo   <sup>2</sup>University of Florida   <sup>3</sup>Harvard Medical School

## Abstract

Diffusion-based generative models have shown promise in synthesizing histopathology images to address data scarcity caused by privacy constraints. Diagnostic text reports provide high-level semantic descriptions, and masks offer fine-grained spatial structures essential for representing distinct morphological regions. However, public datasets lack paired text and mask data for the same histopathological images, limiting their joint use in image generation. This constraint restricts the ability to fully exploit the benefits of combining both modalities for enhanced control over semantics and spatial details. To overcome this, we propose PathDiff, a diffusion framework that effectively learns from unpaired mask-text data by integrating both modalities into a unified conditioning space. PathDiff allows precise control over structural and contextual features, generating high-quality, semantically accurate images. PathDiff also improves image fidelity, text-image alignment, and faithfulness, enhancing data augmentation for downstream tasks like nuclei segmentation and classification. Extensive experiments demonstrate its superiority over existing methods. Our code is published at <https://github.com/bhosalems/PathDiff>.

## 1. Introduction

The recent advancements in computational pathology, driven by deep learning, are revolutionizing the field of histopathology by addressing critical challenges in tasks such as nuclei classification and segmentation [42], survival prediction [44], multi-instance learning [11], and transfer learning [42]. Despite these successes, a significant obstacle persists: the substantial volume of annotated data necessary to effectively train deep learning models. Moreover, the high costs and domain expertise required to annotate such data further ag-

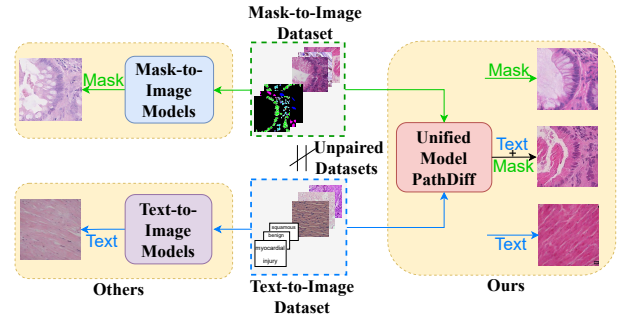


Figure 1. **PathDiff is trained on unpaired datasets**, integrating two conditional modalities —*Text* and *Mask*— to enable versatile image generation. Unlike unimodal conditional models, PathDiff can generate images conditioned on *Text*, *Mask*, or *both*, allowing greater control and adaptability in image synthesis.

gravate this problem. Pathologists must start with low magnification to assess tissue architecture and cellular arrangement, then shift to higher magnification to evaluate finer details such as cell morphology, nucleoli appearance, and chromatin density. Annotating these intricate features is both time-consuming and labor-intensive. For instance, fully annotating the 1k whole slide images from the TCGA dataset<sup>1</sup> [9] would require approximately 40k pathologist hours [16]. Overcoming these limitations is essential to fully unlock the potential of deep learning in histopathology [45].

Generative models in histology [8, 32] have thus emerged as a valuable tool to complement existing datasets, extending beyond traditional data augmentation [10, 28]. More recently, owing to the superior generation quality of diffusion models [6, 19], they are widely used for histological image synthesis, either conditioned on diagnostic text reports [16, 48] or spatial labels such as cell nuclei [34, 35] or regions of interest [1]. However, these existing approaches

<sup>1</sup><https://www.cancer.gov/ccg/research/genome-sequencing/tcga>

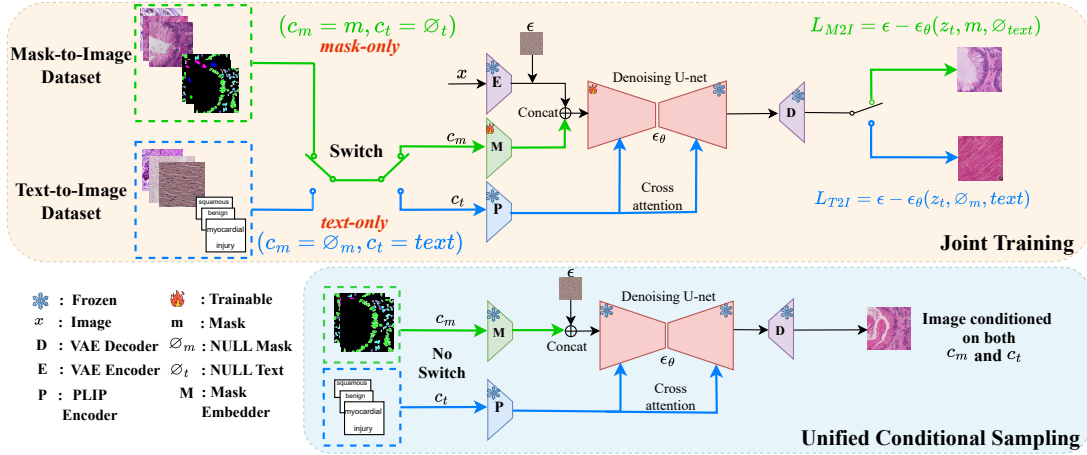


Figure 2. (a) **PathDiff Training Framework:** A training sample is drawn from either the Mask-to-Image (M2I) or the Text-to-Image (T2I) dataset, determined by the probability  $p_{\text{split}}$ , which controls the connection of the Switch. The missing condition in each case is set to  $\emptyset$ . When the Switch selects a sample from the M2I dataset, the Mask-to-Image loss  $L_{M2I}$  is applied; when it selects from the T2I dataset, the Text-to-Image loss  $L_{T2I}$  is used. This approach enables joint training of a single diffusion model on both datasets. (b) **Image Generation:** During generation, both conditions,  $c_m$  (mask) and  $c_t$  (text), are applied to produce samples that unify both conditions.

rely solely on a single modality for conditioning, which limits both the quality of control and the amount of data that can be used.

We recognize the importance of considering text and masks, as they provide complementary information. The text offers contextual knowledge, which varies across cancer types, grades, disease stages, or tissue abnormalities, enabling high-level semantic control over the generation process. In contrast, spatial masks capture local structural details, such as cell shapes and types, providing critical spatial information. Intuitively, simultaneous control of both contextual and spatial information enhances generation. However, no publicly available datasets include open-world text and spatial mask annotations alongside images.

We propose PathDiff, a diffusion framework that unifies text and mask conditions to address the above-mentioned challenges. As shown in Fig. 2, it learns jointly from two independent datasets: one containing image-text pairs and the other containing image-mask pairs. By integrating unpaired text and mask into a single latent space, our model maximizes the use of complementary data and effectively enables generation conditioned on paired text and mask. The main contributions can be summarized as follows:

- To address the data scarcity issue in histology image analysis, we propose a novel diffusion-based framework that unifies unpaired text and masks conditions within a single latent space for complementary knowledge exploration.
- Our pipeline enables joint learning from independent text-image and mask-image datasets, allowing image generation conditioned on both during inference.

- Experiments and qualitative results showcase that our proposed model can effectively integrate the guidance from paired text and mask modalities while the model is trained on unpaired mask and text modalities.
- Owing to the robust and rich joint latent space, empirical evaluations demonstrate that our model outperforms existing approaches across various evaluations, including image fidelity, image-text/mask alignment, and downstream classification and segmentation tasks when conditioned on individual modalities.

## 2. Related Work

Generative adversarial networks [13] have become popular for medical image synthesis [3, 4, 38]; however, they frequently introduce artifacts, particularly in histopathology images [33]. In contrast, diffusion-based methods [19] have demonstrated enhanced image quality in both natural and medical images [33]. Building on this, Classifier Guidance [7] was introduced to condition image generation on specific classes, followed by Classifier-Free Guidance (CFG) [18], which eliminates the need for an auxiliary classifier. Latent Diffusion Models (LDMs) [40] further enhance the computational efficiency, while ControlNet [50] utilizes CFG to introduce multiple spatial controls in Text-to-Image LDMs [40]. Recent approaches for conditional histopathology image generation emphasize text- and mask-based conditioning, which we briefly review in the following sections.

## 2.1. Text to Histopathology Image Synthesis

The application of diffusion models in text-conditioned histopathology image generation remains limited. Summarized reports from the Large Text-Image histopathology dataset TCGA-BRCA [9] were used for text-conditioned image generation in [48] in conjunction with text annotated Tumor-Infiltrating Lymphocyte (TIL) and Tumor probabilities from off the shelf classifiers. Genome sequencing data from the TCGA-BRCA dataset was used in [32], where heavier weights were assigned to earlier steps and lower weights to later steps in the diffusion process to focus on morphological features. Authors in [16] train diffusion model conditioned on Self Supervised Learnt (SSL) embeddings. An auxiliary diffusion model is trained on SSL embedding paired with Quilt [25] image embeddings. At the time of inference, text embeddings are used as proxies for image embedding, allowing for text-to-image synthesis. However, note that none of these methods use mask conditions in conjunction with text.

## 2.2. Mask to Histopathology Image Synthesis

The authors of [1] propose a hierarchical diffusion model to generate large whole-slide images (WSIs) conditioned on synthesized regions of interest. But, this approach does not incorporate fine-grained, cell-level masks. In [35], a text-driven approach is used first to generate cell masks, which, along with their distance maps, are then used to condition histopathology image synthesis. However, this method does not allow for fine-grained control over the spatial placement of the masks. In [49], the diffusion model is trained to synthesize nuclei structures as pixel-level semantic and distance-transform maps, which are then post-processed into instance maps. This is followed by a conditional diffusion model to generate histopathology images. Similarly, [31] introduces a cell-point map to synthesize cell-type masks and images jointly. To tackle class imbalance, [34] employs a Semantic-Diffusion-Model (SDM) [47] for data synthesis, effectively balancing class variance in nuclei datasets.

In contrast, PathDiff uniquely generates histopathology images by unifying mask and text conditions from unpaired datasets, which is beyond the scope of the works discussed above.

## 3. Method

### 3.1. Background

**Diffusion models.** Diffusion Models [19] are generative models that gradually add noise to data through a forward diffusion process, followed by a reverse denoising process that reconstructs the original sample. The forward process corrupts the data sample  $x_0$  through iterative noise addition controlled by a schedule  $\alpha_t$ :

$$q(x_t|x_{t-1}) = \mathcal{N}(x_t; \sqrt{1 - \alpha_t} x_{t-1}, \alpha_t I), \quad (1)$$

where  $\alpha_t$  is a predefined noise schedule. The noisy sample  $x_t$  can be computed by  $x_t = \sqrt{\bar{\alpha}_t} x_0 + \sqrt{1 - \bar{\alpha}_t} \epsilon$ , where  $\bar{\alpha}_t = \prod_{i=1}^t (1 - \alpha_i)$  and  $\epsilon \in \mathcal{N}(0, 1)$  is a random Gaussian noise.

The reverse process, parameterized by a neural network  $p_\theta$ , learns a time-conditioned model to remove the noise added at each step.

Latent Diffusion Models (LDMs) work in a compressed latent space  $z_t$  rather than the high-dimensional data space [40], where the data  $x_0$  is encoded as  $z_0$  through an encoder. LDMs learn to minimize the objective,

$$L = \mathbb{E}_{z_0, t, \epsilon \sim \mathcal{N}(0, 1)} [\|\epsilon - \epsilon_\theta(z_t, t)\|_2^2], \quad (2)$$

where  $\epsilon_\theta$  is the model’s predicted noise at time  $t$ . Owing to the relevance to score-based generation models, the model estimates the log density of the distribution  $z_t$ , i.e.,  $\epsilon_\theta(z_t, t) \approx -\nabla_{z_t} \log p(z_t)$ .

**Classifier-free guidance.** In the denoising process, different conditional inputs  $c$  (text, image, depth, mask, etc.) can be added to control the generation, so the denoising model predicts  $\epsilon_\theta(z_t, t, c)$ . In classifier-free guidance [18], a single neural network is used to parameterize both the unconditional denoising diffusion model  $p_\theta(z)$  and conditional denoising diffusion model  $p_\theta(z|c)$ . While training, with some probability  $p_{\text{uncond}}$ , the unconditional model receives a null token,  $\emptyset$  as  $c$ .  $p_{\text{uncond}}$  is set as a hyperparameter. While sampling, a linear combination of conditional and unconditional score estimates is used:

$$\tilde{\epsilon}_\theta(z_t, t, c) = (1 + w)\epsilon_\theta(z_t, t, c) - w\epsilon_\theta(z_t, t). \quad (3)$$

### 3.2. PathDiff

Histopathology image synthesis requires both high-level semantic guidance and precise structural fidelity. Existing methods [50] often require paired text and mask data, limiting their practicality due to the scarcity of such paired datasets in the histopathology domain. To address these challenges, we propose a unified framework, PathDiff, that leverages unpaired text and mask conditions, enabling fine-grained control over semantic and spatial features. This approach eliminates the need for paired data, supporting flexible and realistic image generation for downstream tasks.

Formally, let  $D_{\text{T2I}} = \{(x_t, c_t)_i\}$  and  $D_{\text{M2I}} = \{(x_m, c_m)_i\}$  represent two unpaired datasets, where  $D_{\text{T2I}}$  consists of image-text pairs and  $D_{\text{M2I}}$  contains image-mask pairs, with no overlapping images between the two datasets. We aim to learn a latent denoising diffusion model  $p_\theta(z_t|t, c_t, c_m)$ . At the inference time,  $p_\theta$  can generate image samples conditioned on text  $c_t$  and mask  $c_m$ .

**Joint training on unpaired datasets.** The training pipeline, illustrated in Fig. 2 (a) and detailed in Algorithm 1, takes as input triplets of noisy latent, conditional mask, and conditional text,  $(x_t, c_m, c_t)$ . We adopt a sampling strategy alternating between T2I and M2I datasets, allowing

the model to learn from both sources and effectively integrate text and mask conditions. Specifically, we jointly train PathDiff by sampling data from the T2I dataset with probability  $p_{\text{split}}$  and from the M2I dataset with probability  $1 - p_{\text{split}}$ . When sampling from  $D_{\text{T2I}}$  dataset, we set  $c_m = \emptyset_m$ , leading to a training triplet of  $(x_t, \emptyset_m, c_t)$ . Similarly, when sampling from  $D_{\text{M2I}}$ , we set  $c_t = \emptyset_t$ , resulting in a training sample of  $(x_m, c_m, \emptyset_t)$ . Following existing methods [40], we set  $\emptyset_t$  as an empty string. For  $\emptyset_m$ , while previous works [34, 35, 47] use a zero vector, we instead use a mask filled with an invalid label, as zero in our dataset indicates a background mask. Additionally, for robustness, we apply unconditional training by setting both  $c_t = \emptyset_t$  and  $c_m = \emptyset_m$  with a small probability  $p_{\text{uncond}}$ , as suggested in [50]. This training pipeline effectively allows PathDiff to learn from both unpaired conditions, enhancing its ability to generate realistic images conditioned on both modalities.

Following ControlNet [50] to add spatial control over image generation, we duplicate parts of the U-Net’s down-sampling and middle layers, adding *zero convolution* layers to these duplicates. Outputs from these layers are integrated into the original U-Net’s skip connections. U-Net was pre-trained on the T2I histopathology dataset before duplicating. The conditional mask is embedded with shallow CNN before being added as input to the U-Net encoder, while text embeddings are extracted from PLIP: pathology CLIP [21] and cross-attended with U-Net layers. We use VAE from [48] trained on the TCGA-BRCA [9] histopathology dataset to encode and decode images. However, as noted by [48], reconstruction loss significantly affects the generation quality; therefore, we study its effect in supplementary. As shown in Fig. 2, all models are frozen except the copied U-Net encoder and shallow mask embedder.

We employ a latent diffusion pipeline [40] to train PathDiff. A shared VAE encoder-decoder is used for both datasets, resulting in a unified latent representation  $z$ . This approach assumes that the VAE can compress and reconstruct images from both datasets without significant loss, maintaining a consistent latent representation across domains.

**Optimization loss.** PathDiff jointly optimizes the diffusion model  $p_\theta$  to predict the noise added at every step  $t$  of the noising process. When the training sample is sampled from  $D_{\text{T2I}}$  it minimizes loss with respect to sample  $x_t \in D_{\text{T2I}}$ ,

$$L_{\text{T2I}} = \mathbb{E}_{z_0, t, \epsilon \sim \mathcal{N}(0,1)} [\|\epsilon - \epsilon_\theta(z_t, t, \emptyset_m, c_t)\|_2^2] \quad (4)$$

similarly, for training samples from  $D_{\text{M2I}}$  it minimizes the loss with respect to sample  $x_m \in D_{\text{M2I}}$ ,

$$L_{\text{M2I}} = \mathbb{E}_{z_0, t, \epsilon \sim \mathcal{N}(0,1)} [\|\epsilon - \epsilon_\theta(z_t, t, c_m, \emptyset_t)\|_2^2] \quad (5)$$

**Unified conditional sampling.** Since PathDiff is jointly trained on both  $D_{\text{T2I}}$  and  $D_{\text{M2I}}$  datasets, it can be queried to sample images conditioned on both  $c_t$  and  $c_m$ , effectively unifying these conditions as guidance, as illustrated

---

### Algorithm 1 Joint Training on Unpaired Datasets

---

**Require:**  $p_{\text{uncond}}$ : probability of unconditional training, Text-to-Image dataset  $D_{\text{T2I}}$ , Mask-to-Image dataset  $D_{\text{M2I}}$ ,  $p_{\text{split}}$ : probability of sampling from  $D_{\text{T2I}}$

```

1: repeat
2:   if  $u \sim \text{Uniform}[0, 1] \geq p_{\text{split}}$  then
3:      $(z_0, c_m = \emptyset_m, c_t) \sim p_1(z_0, c_t)$   $\triangleright$  Sample data from  $D_{\text{T2I}}$ 
4:      $c_t \leftarrow \emptyset_t$  with probability  $p_{\text{uncond}}$   $\triangleright$  Randomly discard text
5:   else
6:      $(z_0, c_m, c_t = \emptyset_t) \sim p_2(z_0, c_m)$   $\triangleright$  Sample data from  $D_{\text{M2I}}$ 
7:      $c_m \leftarrow \emptyset_m$  with probability  $p_{\text{uncond}}$   $\triangleright$  Randomly discard mask
8:      $t \sim \text{Uniform}\{1, \dots, T\}$   $\triangleright$  Sample timestep
9:      $\epsilon \sim \mathcal{N}(\mathbf{0}, \mathbf{I})$   $\triangleright$  Sample noise
10:     $z_t = \sqrt{\alpha_t} z_0 + \sqrt{1 - \alpha_t} \epsilon$   $\triangleright$  Corrupt data
11:    Take gradient step on:
         $\|\epsilon - \epsilon_\theta(z_t, t, c_m, c_t)\|_2^2$  with respect to  $\nabla_\theta$   $\triangleright$  Optimizing PathDiff
12:  until converged

```

---

in Fig. 4 (c) and Fig. 5. The image generation process is illustrated in Fig. 2 (b). For completeness, we include a sampling algorithm in the supplementary. During inference, we generate images using classifier-free guidance [18], updating the predicted noise with the model using Eq. (3). The conditioning variable  $c$  can take values from  $c \in \{(\emptyset_m, c_t), (c_m, \emptyset_t), (c_m, c_t)\}$ . We can selectively generate images from either distribution by setting one of the conditions to  $\emptyset$ . Specifically,

$$z_t \sim \begin{cases} p_\theta(z_t|t, c_t) & \text{if } c = (\emptyset_m, c_t), \\ p_\theta(z_t|t, c_m) & \text{if } c = (c_m, \emptyset_t), \\ p_\theta(z_t|t, c_m, c_t) & \text{if } c = (c_m, c_t). \end{cases}$$

Images generated according to the conditions are illustrated in Fig. 3 and Fig. 4 (b) and Fig. 5. We present extensive experiments on images drawn from each variation of conditions in Sec. 4.

## 4. Experiments

We evaluate our method in two main aspects: the quality of the generated images and the effectiveness of using synthetic images as additional training data for downstream task. We evaluate image generation quality in Sec. 4.3, focusing on image fidelity, image-mask faithfulness, and alignment quality between images and text. Additionally, the utility of the synthetic images in downstream segmentation tasks is detailed in Sec. 4.4. We also discuss the domain experts’ survey results in the supplementary. PathDiff was jointly trained on M2I and T2I datasets; however, we can generate images conditioned on text, mask, or both. Each of these variants is evaluated separately. ControlNet [50] uses SD [40] backbone pre-trained on the T2I dataset for further fine-tuning on the M2I dataset. Therefore, ControlNet is also evaluated in two variants for a fair and inclusive comparison.



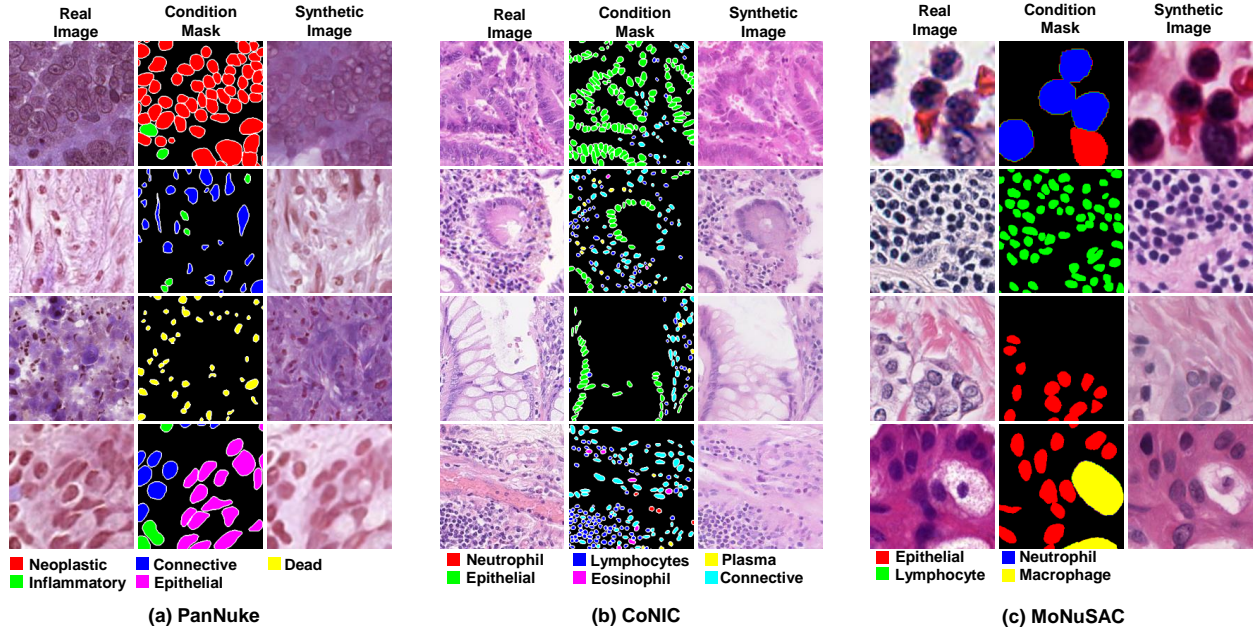


Figure 3. **Synthetic images generated by PathDiff on Mask to Image datasets** (a) PanNuke [12], (b) CoNIC [15], (c) MoNuSAC [46]. PathDiff closely follows the spatial structures defined by the cell type label map, producing synthetic images that closely resemble the spatial arrangement of real images.

Method	Condition Modality (Train, Sample)	PanNuke				CoNIC				MoNuSAC			
		Train		Test		Train		Test		Train		Test	
		FID ↓	KID ↓	FID ↓	KID ↓	FID ↓	KID ↓	FID ↓	KID ↓	FID ↓	KID ↓	FID ↓	KID ↓
Diffmix [34]	(Mask, Mask)	7.28	<u>0.0492</u>	8.32	<u>0.0536</u>	8.09	0.0966	8.58	0.0937	9.25	<u>0.1036</u>	16.78	0.35
SDM [47]	(Mask, Mask)	<u>7.14</u>	0.1147	<b>7.13</b>	0.1149	8.27	<u>0.0709</u>	9.80	0.0737	<u>7.46</u>	0.1278	<u>9.44</u>	0.1340
ControlNet [50]	(Mask+Text, Mask)	16.44	0.0705	15.36	0.7722	<u>6.76</u>	0.0790	<u>6.79</u>	<u>0.0695</u>	20.06	0.1050	20.56	<u>0.1068</u>
PathDiff	(Mask+Text, Mask)	<b>6.94</b>	<b>0.0389</b>	<u>7.21</u>	<b>0.0415</b>	<b>5.64</b>	<b>0.0524</b>	<b>5.54</b>	<b>0.0488</b>	<b>6.71</b>	<b>0.0616</b>	<b>6.99</b>	<b>0.0758</b>

Table 1. **Comparison of CLIP-FID and KID across training and test splits** for PanNuke [12], CoNIC [15], and MoNuSAC [46]. PathDiff is trained jointly with T2I dataset: PathCap [43]. ControlNet [50] uses SD [40] backbone trained on the PathCap dataset. The best results are in **bold** and the second best is underlined.

#### 4.1. Datasets

We use three mask-image histopathology datasets (PanNuke [12], CoNIC [15], and MoNuSAC [46]) and one text-image dataset (PathCap [43]) to conduct a comparative analysis across multiple metrics, evaluating various diffusion methods and their related downstream tasks.

PanNuke dataset [12] provides annotated histopathology images across 19 tissue types with 189,744 annotated nuclei in five classes (neoplastic, inflammatory, connective, dead, and epithelial). The dataset is highly imbalanced [23] and one of the most challenging to perform the segmentation task [26].

CoNIC dataset [15] is one of the most extensive publicly available histopathology datasets, containing approximately

535,000 labeled colon nuclei across six cell types: epithelial, lymphocytes, plasma cells, eosinophils, neutrophils, and connective tissue cells.

MoNuSAC [46] spans four organs (lung, prostate, kidney, and breast) and includes over 46,000 annotated nuclear boundaries collected from diverse sources for four cell types: epithelial cells, lymphocytes, macrophages, and neutrophils.

PathCap [43] includes 207K pathology image-caption pairs, 197K from PubMed and guidelines, and 10K annotated by expert cytologists in liquid-based cytology (LBC). PathCap has diverse Pan-Cancer image-text pairs spanning multiple organs, making it suitable for joint training. We used a 100K subset of PathCap containing only H&E-stained histology images to ensure consistency with the three mask-

Method	PanNuke		CoNIC		MoNuSAC	
	FS1 $\uparrow$	FS2 $\uparrow$	FS1 $\uparrow$	FS2 $\uparrow$	FS1 $\uparrow$	FS2 $\uparrow$
Diffmix [34]	0.7419	0.6964	0.7597	0.7163	0.6488	0.6182
SDM [47]	0.7025	0.6826	0.7433	0.7376	0.6377	0.6104
ControlNet [50]	0.6990	0.6821	0.7629	0.7537	0.6317	0.6081
PathDiff	<b>0.7437</b>	<b>0.7406</b>	<b>0.7873</b>	<b>0.7632</b>	<b>0.6519</b>	<b>0.6308</b>

Table 2. **Faithfulness scores** for the PanNuke [12], CoNIC [15], and MoNuSAC [46] datasets. FS1 measures the adherence of synthetic images to the spatial structure of real masks by computing  $\text{DICE}(M_{syn}^{pred}, M_{real})$ . At the same time, FS2 assesses the similarity between synthetic and real images for potential downstream tasks, calculated as  $\text{DICE}(M_{syn}^{pred}, M_{real}^{pred})$ .

image datasets, which are also H&E-stained.

**Data splits:** All datasets use an 80:20 train/test split, applied consistently to both generation and downstream evaluations. Synthetic examples for downstream task are drawn only from the conditions training split and added during model training to ensure fair comparisons.

## 4.2. Implementation Details

PathDiff is trained on  $256 \times 256$  image patches. We resize patches for the MoNuSAC [46] and PathCap [43] datasets by taking crops of size  $256 \times 256$  from WSIs. PanNuke [12] and CoNIC [15] datasets originally have images with size  $256 \times 256$ . Our model is trained for 60 epochs on 4 NVIDIA A6000 GPUs with a batch size of 72 and a learning rate of  $3.75 \times 10^{-5}$  with 1000 warmup steps. We use DDIM sampling [41] with 200 steps and a classifier-free guidance scale set to 1.75 for image generation. We train CellViT on a single NVIDIA RTX A6000 for 130 epochs (with the first 30 epochs frozen), using a batch size of 16 and a learning rate of 0.001, retaining all other training parameters from the original work [23].

## 4.3. Image Generation Quality

**Image Generation Fidelity:** To evaluate the quality of generated images, we use CLIP-FID following [16, 37]. We additionally report Kernel Inception Distance (KID) [2] to provide an unbiased estimate. As shown in Tab. 1, PathDiff achieves the best generation quality in terms of FID and KID compared against the existing mask-to-image generation methods: Diffmix [34], SDM [47] and ControlNet [50]. Fig. 3 presents qualitative examples generated with the guidance of mask conditions.

**Mask-to-Image Faithfulness:** To evaluate whether the generated images adhere to the spatial guidance provided by the masks, we use the evaluation protocol of SPADE [36], also termed as Faithfulness Score (FS) [27]. Auxiliary segmentation model [23]  $S$  is trained on a train split of mask-image datasets. Real images  $I_{real}$  from test split  $(I_{real}, M_{real})$  are passed through  $S$  to get predicted segmentation masks  $M_{real}^{pred}$ . Synthetic images generated by

our model conditioned on masks  $M_{real}$  are passed through  $S$  to get predicted segmentation masks  $M_{syn}^{pred}$ . FS1 calculates  $\text{DICE}(M_{syn}^{pred}, M_{real})$ , FS2 on other hand calculates  $\text{DICE}(M_{syn}^{pred}, M_{real}^{pred})$ . As shown in Tab. 2, we attain the best FS1 and FS2 among methods, indicating that the synthetic images closely align with the real masks and reach similarity to real images, enhancing their utility for downstream segmentation tasks. Notably, compared with the counterparts [34, 47, 50], which also sample from the single mask condition, the joint training strategy demonstrates a superior ability to learn from the limited data.

**Text-to-Image Alignment:** Fig. 4(b) presents qualitative samples generated by our model conditioned only on text; images generated replicate visual attributes about the text as observed in real images. Tab. 3 presents FID and KID scores compared to ControlNet [50] conditioned only on text. We also use metric - **PLIP** [21] **cosine similarity** to evaluate the consistency between image and text embeddings. High PLIP image similarity scores indicate better alignment between text and images. PathDiff has the highest PLIP score of  $\geq 24.66$ , indicating good alignment between texts and generated images. Our model performs better than ControlNet on FID [17] and KID [2] across all M2I constituent datasets, indicating large T2I datasets can be jointly trained with a wide range of M2I datasets.

**Unified Sampling Evaluation:** No public dataset currently provides (text, mask, image) triplets, which complicates the evaluation of unified conditional sampling. In medical imaging, silver-standard masks [30] often replace human (golden-standard) annotations when such labels are unavailable. We use DeepCMorph [24]—an encoder-decoder model extensively trained on heterogeneous data—to generate silver-standard masks for PathCap. These masks, combined with PathCap text, form triplets for inference and evaluation. Because CONIC [15] covers all nuclei types targeted by DeepCMorph, we employ its checkpoints for these experiments. To check whether the masks generated by DeepCMorph are reasonable, we randomly pair the text in PathCap with masks in the CONIC dataset and use this pairing as conditions for a generation, as indicated by PathDiff-R.

In Tab. 4, PathDiff and ControlNet rely on silver-standard masks from PathCap. Even with random pairing, PathDiff-R surpasses ControlNet in FID while maintaining a similar PLIP score. PathDiff attains the best FID and PLIP results, indicating a meaningful pairing of silver-standard masks with text. Furthermore, comparing PathDiff’s FID on CONIC in Tab. 3 to the metrics in Tab. 4 shows that a joint conditioning space yields richer images with improved FID values while preserving text-image similarity, as reflected by a comparable PLIP score. The approach still yields a performance boost even with these silver-standard masks. Note that the models have never seen silver standard masks

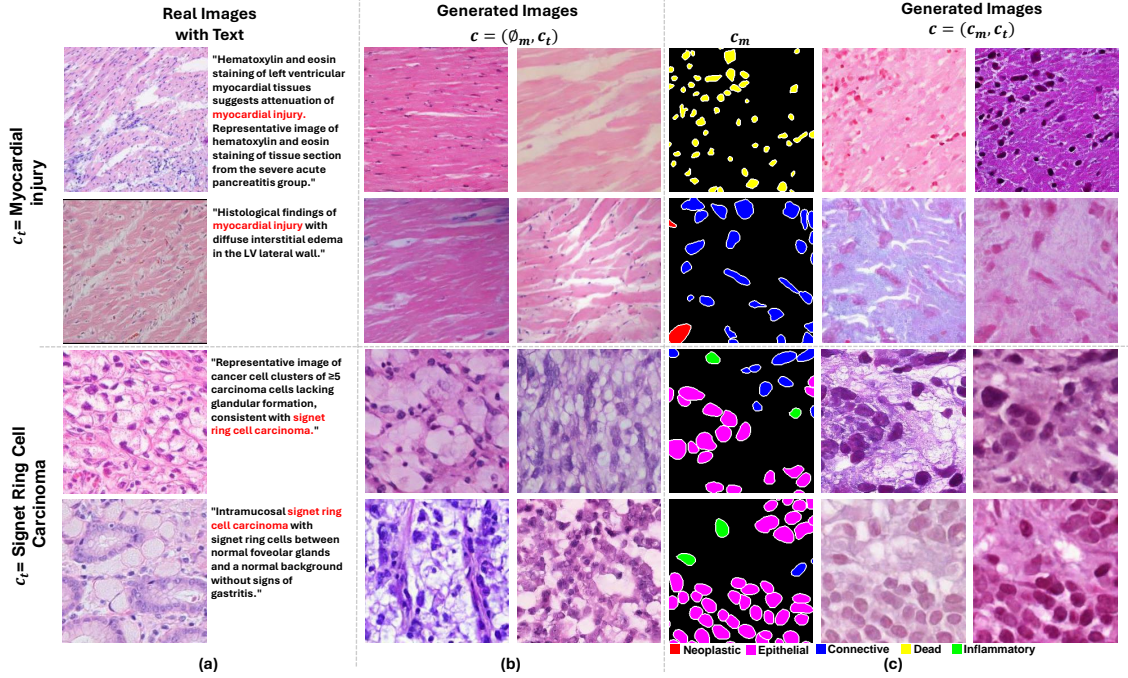


Figure 4. **Qualitative examples demonstrate the effectiveness of unifying guidance from random pairings of text and mask conditions.** (a) Real images are shown with their respective text-based descriptions. (b) PathDiff generated images conditioned solely on text replicate the visual attributes observed in real images, with the mask condition set to  $\emptyset_m$ . (c) PathDiff-generated images conditioned on the same text  $c_t$  and an additional mask  $c_m$  accurately incorporate the visual features of the real images and adhere to the specified cell mask structure.

Method	Condition Modality	M2I Dataset: PanNuke						M2I Dataset: CoNIC						M2I Dataset: MoNuSAC					
		Train			Test			Train			Test			Train			Test		
		(Train,Sample)	FID ↓	KID ↓	PLIP ↑	FID ↓	KID ↓	PLIP ↑	FID ↓	KID ↓	PLIP ↑	FID ↓	KID ↓	PLIP ↑	FID ↓	KID ↓	PLIP ↑	FID ↓	KID ↓
ControlNet [50]	(Mask+Text,Text)	45.39	0.0872	23.27	45.04	0.0886	22.95	26.32	0.1275	21.97	25.10	0.1269	21.98	28.66	0.1111	21.88	29.86	0.1091	21.76
PathDiff	(Mask+Text,Text)	18.52	0.0619	24.18	19.60	0.0644	24.05	18.97	0.0640	24.03	19.96	0.0655	24.17	13.72	0.0538	24.17	14.04	0.0557	24.66

Table 3. **Comparison of CLIP-FID, KID, and PLIP similarity scores** for training and test splits for text-image dataset: PathCap. PathDiff is jointly trained with three M2I datasets: PanNuke [12], CoNIC [15], and MoNuSAC [46]. PLIP similarity scores on real PathCap [43] train and test splits are **26.34** and **26.56**, respectively, as a reference for the comparison.

Data Domain	Condition Modality	FID ↓	KID ↓	PLIP ↑
ControlNet	(Mask+Text, Mask+Text)	15.72	<b>0.0699</b>	22.03
PathDiff-R	(Mask+Text, Mask+Text)	11.12	0.1059	22.09
PathDiff	(Mask+Text, Mask+Text)	<b>10.54</b>	0.0766	<b>24.02</b>

Table 4. **Comparison of CLIP-FID, KID, and PLIP scores using text-silver standard mask pairs versus random text-mask pairs.** Text is drawn from PathCap [43], with masks predicted by DeepCMorph [24]. Random pairings use masks from CONIC [15] and texts from PathCap. Both ControlNet [50] and PathDiff rely on silver standard masks, whereas PathDiff-R uses random pairings.

of the PathCap dataset in the training process. Fig. 5 shows faithful image generation with silver standard masks and texts.

#### 4.4. Downstream tasks

To evaluate the utility of the generated images, we use them as additional training data for the segmentation model. Cel-IViT [20] (SAM-B variant) backbone with HoVer-Net [14] as decoder. Tab. 5 compares segmentation and classification performance in multiple metrics, including Dice, Jaccard, AJI (Aggregated Jaccard Index), HD95 [22] (95th percentile Hausdorff Distance), F1 score, precision and recall. We note that our proposed method consistently improves the performance across various metrics on all three datasets. In segmentation tasks on PanNuke, PathDiff trained on real and synthetic data achieves the highest Dice score (0.8164) and performs well across other metrics like Jaccard (0.7122) and AJI (0.7117). Similarly, in classification tasks on PanNuke, PathDiff achieves a strong F1 score of 0.8161 with balanced precision and recall. On the CoNIC dataset, PathDiff again



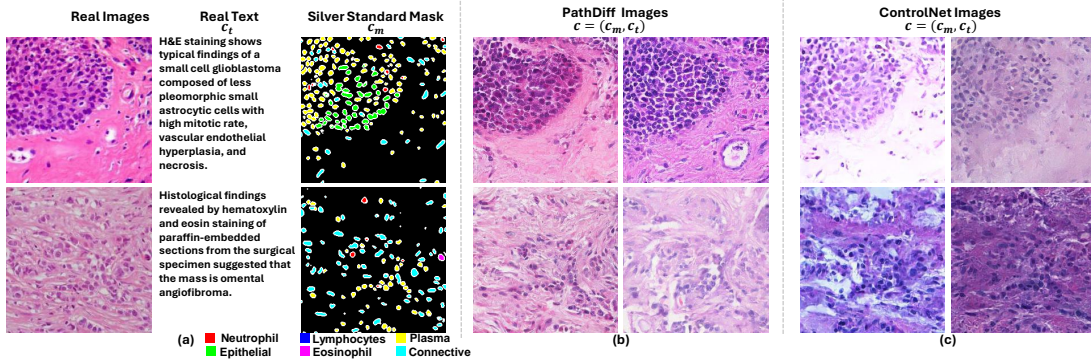


Figure 5. Qualitative examples demonstrate the effectiveness of unifying guidance from paired text and silver standard masks generated by [24] from PathCap dataset [43] (a) Real images and Text with silver masks (b) PathDiff generated images (c) ControlNet generated images.

Dataset	Method	Train Data	Segmentation				Classification		
			Dice $\uparrow$	Jaccard $\uparrow$	AJI $\uparrow$	HD (95) $\downarrow$	F1 $\uparrow$	Precision $\uparrow$	Recall $\uparrow$
PanNuke	Baseline	Real	0.7834	0.6951	0.6904	6.81	0.7826	0.7472	<u>0.8215</u>
	w/ SDM	Real+Synth	0.7891	0.6816	0.6729	6.26	0.7792	<u>0.8014</u>	0.7581
	w/ ControlNet [50]	Real+Synth	<u>0.8093</u>	<u>0.6979</u>	0.6954	<u>5.87</u>	<u>0.8134</u>	<b>0.8354</b>	0.7925
	w/ PathDiff	Synth	0.7311	0.6538	0.6539	7.73	0.7140	0.7039	0.7244
	w/ PathDiff	Real+Synth	<b>0.8164</b>	<b>0.7122</b>	<b>0.7117</b>	<b>5.12</b>	<b>0.8161</b>	0.7827	<b>0.8524</b>
CoNIC	Baseline	Real	0.7927	0.6978	0.6917	4.38	0.7614	0.7153	0.8138
	w/ SDM	Real+Synth	0.8007	0.6846	0.6846	4.50	0.7883	0.7620	<u>0.8164</u>
	w/ ControlNet [50]	Real+Synth	<u>0.8076</u>	<u>0.6999</u>	<u>0.6950</u>	3.16	<u>0.8000</u>	<b>0.8344</b>	0.7683
	w/ PathDiff	Synth	0.7612	0.6480	0.6473	6.37	0.7449	0.7783	0.8107
	w/ PathDiff	Real+Synth	<b>0.8356</b>	<b>0.7195</b>	<b>0.7141</b>	<b>2.97</b>	<b>0.8053</b>	<u>0.7790</u>	<b>0.8328</b>
MoNuSAC	Baseline	Real	<u>0.7089</u>	<u>0.6131</u>	<u>0.6097</u>	6.77	0.6652	0.6383	0.6944
	w/ SDM	Real+Synth	0.6783	0.5744	0.5731	<u>6.49</u>	0.6685	<u>0.6940</u>	0.6448
	w/ ControlNet [50]	Real + Synth	0.6940	0.5852	0.5800	6.54	0.6843	0.6533	0.7183
	w/ PathDiff	Synth	0.6671	0.5894	0.5894	7.07	<u>0.6851</u>	0.6345	<b>0.7445</b>
	w/ PathDiff	Real+Synth	<b>0.7221</b>	<b>0.6197</b>	<b>0.6192</b>	<b>5.88</b>	<b>0.7115</b>	<b>0.6951</b>	<u>0.7286</u>

Table 5. Comparison of segmentation and classification metrics across different datasets and methods on the CellViT model. The Baseline is trained with real data, and the rest of the methods have synthetic data added in equal proportion to the train set.

leads in segmentation with a Dice score of 0.8356 and performs well in classification with an F1 score of 0.8053. On MoNuSAC, where performance is generally lower across all methods, PathDiff still outperforms others in segmentation with a Dice score of 0.7221 and achieves an F1 score of 0.7115 for classification. Importantly, training solely with synthetic images still achieves performance comparable to the baseline. This outcome suggests that the synthetic images are robust and simulate the original data effectively. It is pertinent to mention that when evaluating the classification and segmentation performance, the split used included only real test data.

## 5. Conclusion

To address data scarcity in histopathology image analysis, we propose a novel diffusion framework that simultaneously leverages diagnostic reports as contextual guidance and mask inputs for precise spatial control. Incorporating these two components ensures more accurate and meaningful image generation, especially when high-quality annotated data is limited. We show that a joint conditional diffusion model can unify conditions from unpaired data. At inference, classifier-free guidance generates images conditioned on both modalities, addressing data scarcity challenges. This approach optimizes the use of existing data, achieving superior results in both image quality and downstream tasks like segmentation and classification.



## References

- [1] Marco Aversa, Gabriel Nobis, Miriam Hägele, Kai Standvoss, Mihaela Chirica, Roderick Murray-Smith, Ahmed Alaa, Lukas Ruff, Daniela Ivanova, Wojciech Samek, Frederick Klauschen, Bruno Sanguinetti, and Luis Oala. Diffinfinite: Large mask-image synthesis via parallel random patch diffusion in histopathology. In *Thirty-seventh Conference on Neural Information Processing Systems Datasets and Benchmarks Track*, 2023. 1, 3
- [2] Mikołaj Bińkowski, Dougal J. Sutherland, Michael Arbel, and Arthur Gretton. Demystifying MMD GANs. In *International Conference on Learning Representations*, 2018. 6, 13
- [3] S. Butte, H. Wang, A. Vakanski, and M. Xian. Enhanced sharp-gan for histopathology image synthesis. In *Proceedings of IEEE International Symposium on Biomedical Imaging (ISBI)*, page 10.1109/isbi53787.2023.10230516, 2023. Epub 2023 Sep 1. 2
- [4] Gagandeep B. Daroach, Savannah R. Duenweg, Michael Brehler, Allison K. Lowman, Kenneth A. Iczkowski, Kenneth M. Jacobsohn, Josiah A. Yoder, and Peter S. LaViolette. Prostate cancer histology synthesis using stylegan latent space annotation. In *Medical Image Computing and Computer Assisted Intervention – MICCAI 2022*, pages 398–408, Cham, 2022. Springer Nature Switzerland. 2
- [5] Jia Deng, Wei Dong, Richard Socher, Li-Jia Li, Kai Li, and Li Fei-Fei. Imagenet: A large-scale hierarchical image database. In *2009 IEEE conference on computer vision and pattern recognition*, pages 248–255. Ieee, 2009. 12
- [6] Prafulla Dhariwal and Alexander Nichol. Diffusion models beat gans on image synthesis. In *Advances in Neural Information Processing Systems*, pages 8780–8794. Curran Associates, Inc., 2021. 1
- [7] Prafulla Dhariwal and Alex Nichol. Diffusion models beat gans on image synthesis. In *Proceedings of the 35th International Conference on Neural Information Processing Systems*, Red Hook, NY, USA, 2024. Curran Associates Inc. 2
- [8] James M. Dolezal, Rachelle Wolk, Hanna M. Hieromnimon, Frederick M. Howard, Andrew Srisuwananukorn, Dmitry Karpeyev, Siddhi Ramesh, Sara Kochanny, Jung Woo Kwon, Meghana Agni, et al. Deep learning generates synthetic cancer histology for explainability and education. *NPJ Precision Oncology*, 7(1):49, 2023. 1
- [9] JN Cancer Genome Atlas Research Network et al. The cancer genome atlas pan-cancer analysis project. *Nature Genetics*, 45(10):1113–1120, 2013. 1, 3, 4, 17
- [10] Virginia Fernandez, Walter Hugo Lopez Pinaya, Pedro Borges, Petru-Daniel Tudosi, Mark S. Graham, Tom Vercauteren, and M. Jorge Cardoso. Can segmentation models be trained with fully synthetically generated data? In *Simulation and Synthesis in Medical Imaging: 7th International Workshop, SASHIMI 2022, Held in Conjunction with MICCAI 2022, Singapore, September 18, 2022, Proceedings*, pages 79–90. Springer, 2022. 1
- [11] Michael Gadermayr and Maximilian Tschuchnig. Multiple instance learning for digital pathology: A review of the state-of-the-art, limitations & future potential. *Computerized Medical Imaging and Graphics*, 112:102337, 2024. 1
- [12] Jevgenij Gamper, Navid Alemi Koohbanani, Ksenija Benet, Ali Khuram, and Nasir Rajpoot. Pannuke: An open pan-cancer histology dataset for nuclei instance segmentation and classification. In *Digital Pathology*, pages 11–19, Cham, 2019. Springer International Publishing. 5, 6, 7, 12, 13, 14, 15, 17, 18
- [13] Ian Goodfellow, Jean Pouget-Abadie, Mehdi Mirza, Bing Xu, David Warde-Farley, Sherjil Ozair, Aaron Courville, and Yoshua Bengio. Generative adversarial nets. In *Advances in neural information processing systems*, pages 2672–2680, 2014. 2
- [14] Simon Graham, Quoc Dang Vu, Shan E Ahmed Raza, Ayesha Azam, Yee Wah Tsang, Jin Tae Kwak, and Nasir Rajpoot. Hover-net: Simultaneous segmentation and classification of nuclei in multi-tissue histology images. *Medical image analysis*, 58:101563, 2019. 7
- [15] Simon Graham, Quoc Dang Vu, Mostafa Jahanifar, Martin Weigert, Uwe Schmidt, Wenhua Zhang, Jun Zhang, Sen Yang, Jinxi Xiang, Xiyue Wang, et al. Conic challenge: Pushing the frontiers of nuclear detection, segmentation, classification and counting. *Medical image analysis*, 92:103047, 2024. 5, 6, 7, 12, 14, 17
- [16] Alexandros Graikos, Srikanth Yellapragada, Minh-Quan Le, Saarthak Kapse, Prateek Prasanna, Joel Saltz, and Dimitris Samaras. Learned representation-guided diffusion models for large-image generation. In *Proceedings of the IEEE/CVF Conference on Computer Vision and Pattern Recognition*, pages 8532–8542, 2024. 1, 3, 6, 17
- [17] Martin Heusel, Hubert Ramsauer, Thomas Unterthiner, Bernhard Nessler, and Sepp Hochreiter. Gans trained by a two time-scale update rule converge to a local nash equilibrium. In *Advances in Neural Information Processing Systems*. Curran Associates, Inc., 2017. 6, 12, 13, 15
- [18] Jonathan Ho and Tim Salimans. Classifier-free diffusion guidance, 2022. 2, 3, 4
- [19] Jonathan Ho, Ajay Jain, and Pieter Abbeel. Denoising diffusion probabilistic models. In *Advances in Neural Information Processing Systems*, pages 6840–6851, 2020. 1, 2, 3
- [20] Fabian Hörst, Moritz Rempe, Lukas Heine, Constantin Seibold, Julius Keyl, Giulia Baldini, Selma Ugurel, Jens Siveke, Barbara Grünwald, Jan Egger, et al. Cellvit: Vision transformers for precise cell segmentation and classification. *Medical Image Analysis*, 94:103143, 2024. 7
- [21] Zhi Huang, Federico Bianchi, Mert Yuksekogun, Thomas J Montine, and James Zou. A visual-language foundation model for pathology image analysis using medical twitter. *Nature Medicine*, pages 1–10, 2023. 4, 6, 13, 15
- [22] Daniel P Huttenlocher, Gregory A. Klanderman, and William J Rucklidge. Comparing images using the hausdorff distance. *IEEE Transactions on pattern analysis and machine intelligence*, 15(9):850–863, 1993. 7
- [23] Fabian Hörst, Moritz Rempe, Lukas Heine, Constantin Seibold, Julius Keyl, Giulia Baldini, Selma Ugurel, Jens Siveke, Barbara Grünwald, Jan Egger, and Jens Kleesiek. Cellvit: Vision transformers for precise cell segmentation and classification. *Medical Image Analysis*, 94:103143, 2024. 5, 6, 12

- [24] Andrey Ignatov, Josephine Yates, and Valentina Boeva. Histopathological image classification with cell morphology aware deep neural networks. In *Proceedings of the IEEE/CVF Conference on Computer Vision and Pattern Recognition*, pages 6913–6925, 2024. [6](#), [7](#), [8](#)
- [25] Wisdom Oluchi Ikezogwo, Mehmet Saygin Seyfioglu, Fate-meh Ghezloo, Dylan Stefan Chan Geva, Fatwir Sheikh Mohammed, Pavan Kumar Anand, Ranjay Krishna, and Linda Shapiro. Quilt-1m: One million image-text pairs for histopathology. *arXiv preprint arXiv:2306.11207*, 2023. [3](#)
- [26] Talha Ilyas, Zubaer Ibna Mannan, Abbas Khan, Sami Azam, Hyongsuk Kim, and Friso De Boer. Tsfd-net: Tissue specific feature distillation network for nuclei segmentation and classification. *Neural Networks*, 151:1–15, 2022. [5](#)
- [27] Nicholas Konz, Yuwen Chen, Haoyu Dong, and Maciej A. Mazurowski. Anatomically-controllable medical image generation with segmentation-guided diffusion models. In *Proceedings of the Medical Image Computing and Computer Assisted Intervention – MICCAI 2024*, page pending. Springer Nature Switzerland, 2024. Accepted. [6](#)
- [28] Adrian B. Levine, Jason Peng, David Farnell, Mitchell Nursey, Yiping Wang, Julia R. Naso, Hezhen Ren, Hossein Farahani, Colin Chen, Derek Chiu, Aline Talhouk, Brandon Sheffield, Maziar Riazzy, Philip P. Ip, Carlos Parra-Herran, Anne Mills, Naveena Singh, Basile Tessier-Cloutier, Taylor Salisbury, Jonathan Lee, Tim Salcudean, Steven J. M. Jones, David G. Huntsman, C. Blake Gilks, Stephen Yip, and Ali Bashashati. Synthesis of diagnostic quality cancer pathology images by generative adversarial networks. *The Journal of Pathology*, 252(2):178–188, 2020. [1](#)
- [29] Ming Y Lu, Bowen Chen, Drew FK Williamson, Richard J Chen, Ivy Liang, Tong Ding, Guillaume Jaume, Igor Odintsov, Long Phi Le, Georg Gerber, et al. A visual-language foundation model for computational pathology. *Nature Medicine*, 30:863–874, 2024. [13](#)
- [30] O. Lucena, R. Souza, L. Rittner, R. Frayne, and R. Lotufo. Convolutional neural networks for skull-stripping in brain mr imaging using silver standard masks. *Artificial Intelligence in Medicine*, 98:48–58, 2019. [6](#)
- [31] Seonghui Min, Hyun-Jic Oh, and Won-Ki Jeong. Co-synthesis of histopathology nuclei image-label pairs using a context-conditioned joint diffusion model. In *Computer Vision – ECCV 2024*, pages 146–162, Cham, 2025. Springer Nature Switzerland. [3](#), [12](#)
- [32] Puria Azadi Moghadam, Sanne Van Dalen, Karina C. Martin, Jochen Lennerz, Stephen Yip, Hossein Farahani, and Ali Bashashati. A morphology focused diffusion probabilistic model for synthesis of histopathology images. In *2023 IEEE/CVF Winter Conference on Applications of Computer Vision (WACV)*, pages 1999–2008, 2023. [1](#), [3](#)
- [33] G. Müller-Franzes, J.M. Niehues, F. Khader, et al. A multi-modal comparison of latent denoising diffusion probabilistic models and generative adversarial networks for medical image synthesis. *Scientific Reports*, 13:12098, 2023. [2](#)
- [34] Hyun-Jic Oh and Won-Ki Jeong. Diffmix: Diffusion model-based data synthesis for nuclei segmentation and classification in imbalanced pathology image datasets. In *Medical Image Computing and Computer Assisted Intervention – MICCAI 2023: 26th International Conference, Vancouver, BC, Canada, October 8–12, 2023, Proceedings, Part III*, page 337–345, Berlin, Heidelberg, 2023. Springer-Verlag. [1](#), [3](#), [4](#), [5](#), [6](#), [12](#), [14](#), [18](#)
- [35] Hyun-Jic Oh and Won-Ki Jeong. Controllable and efficient multi-class pathology nuclei data augmentation using text-conditioned diffusion models. In *Medical Image Computing and Computer Assisted Intervention – MICCAI 2024*, pages 36–46, Cham, 2024. Springer Nature Switzerland. [1](#), [3](#), [4](#)
- [36] Taesung Park, Ming-Yu Liu, Ting-Chun Wang, and Jun-Yan Zhu. Semantic image synthesis with spatially-adaptive normalization. In *Proceedings of the IEEE Conference on Computer Vision and Pattern Recognition*, 2019. [6](#)
- [37] Gaurav Parmar, Richard Zhang, and Jun-Yan Zhu. On aliased resizing and surprising subtleties in gan evaluation. In *CVPR*, 2022. [6](#)
- [38] Adalberto Claudio Quiros, Roderick Murray-Smith, and Ke Yuan. Pathologygan: Learning deep representations of cancer tissue. In *Proceedings of the Third Conference on Medical Imaging with Deep Learning*, pages 669–695. PMLR, 2020. [2](#)
- [39] Alec Radford, Jong Wook Kim, Chris Hallacy, Aditya Ramesh, Gabriel Goh, Sandhini Agarwal, Girish Sastry, Amanda Askell, Pamela Mishkin, Jack Clark, Gretchen Krueger, and Ilya Sutskever. Learning transferable visual models from natural language supervision. *CoRR*, abs/2103.00020, 2021. [13](#), [15](#)
- [40] Robin Rombach, Andreas Blattmann, Dominik Lorenz, Patrick Esser, and Björn Ommer. High-resolution image synthesis with latent diffusion models, 2021. [2](#), [3](#), [4](#), [5](#), [17](#), [18](#)
- [41] Jiaming Song, Chenlin Meng, and Stefano Ermon. Denoising diffusion implicit models. *arXiv:2010.02502*, 2020. [6](#)
- [42] Chetan L. Srinidhi, Ozan Ciga, and Anne L. Martel. Deep neural network models for computational histopathology: A survey. *Medical Image Analysis*, 67:101813, 2021. [1](#)
- [43] Yuxuan Sun, Chenglu Zhu, Sunyi Zheng, Kai Zhang, Lin Sun, Zhongyi Shui, Yunlong Zhang, Honglin Li, and Lin Yang. Pathasst: A generative foundation ai assistant towards artificial general intelligence of pathology. *Proceedings of the AAAI Conference on Artificial Intelligence*, 38:5034–5042, 2024. [5](#), [6](#), [7](#), [8](#), [13](#), [15](#), [16](#), [17](#), [18](#)
- [44] Luís A. Vale-Silva and Karl Rohr. Long-term cancer survival prediction using multimodal deep learning. *Scientific Reports*, 11(1):13505, 2021. Epub 2021 Jun 29. [1](#)
- [45] Gregory Verghese, Jochen K. Lennerz, Danny Ruta, Wen Ng, Selvam Thavaraj, Kalliopi P. Siziopikou, Threnesan Naidoo, Swapnil Rane, Roberto Salgado, Sarah E. Pinder, and Anita Grigoriadis. Computational pathology in cancer diagnosis, prognosis, and prediction - present day and prospects. *The Journal of Pathology*, 260(5):551–563, 2023. Epub 2023 Aug 14. [1](#)
- [46] Ruchika Verma, Neeraj Kumar, Abhijeet Patil, Nikhil Cherian Kurian, Swapnil Rane, and Amit Sethi. Multi-organ nuclei segmentation and classification challenge 2020. *IEEE transactions on medical imaging*, 39(1380-1391):8, 2020. [5](#), [6](#), [7](#), [12](#), [14](#), [17](#)

- [47] Weilun Wang, Jianmin Bao, Wengang Zhou, Dongdong Chen, Dong Chen, Lu Yuan, and Houqiang Li. Semantic image synthesis via diffusion models, 2022. [3](#), [4](#), [5](#), [6](#), [12](#), [14](#)
- [48] Srikar Yellapragada, Alexandros Graikos, Prateek Prasanna, Tahsin Kurc, Joel Saltz, and Dimitris Samaras. Pathldm: Text conditioned latent diffusion model for histopathology. In *Proceedings of the IEEE/CVF Winter Conference on Applications of Computer Vision (WACV)*, pages 5182–5191, 2024. [1](#), [3](#), [4](#), [17](#)
- [49] Xinyi Yu, Guanbin Li, Wei Lou, Siqi Liu, Xiang Wan, Yan Chen, and Haofeng Li. Diffusion-based data augmentation for nuclei image segmentation. In *Medical Image Computing and Computer Assisted Intervention – MICCAI 2023*, pages 592–602, Cham, 2023. Springer Nature Switzerland. [3](#)
- [50] Lvmin Zhang, Maneesh K. Wu, Weiyang Zeng, Yuxin Zhang, Hussain Salman, and Vladlen Koltun. Adding conditional control to text-to-image diffusion models. *arXiv preprint arXiv:2302.05543*, 2023. [2](#), [3](#), [4](#), [5](#), [6](#), [7](#), [8](#), [12](#), [14](#), [16](#), [17](#)

# PathDiff: Histopathology Image Synthesis with Unpaired Text and Mask Conditions

## Supplementary Material

### 6. Scaling Augmentation in Downstream Tasks

To evaluate the impact of synthetic data augmentation on downstream tasks, we designed three augmented sets for training the CellViT [23] model on the PanNuke [12] dataset. These augmented datasets were generated from the training split, conditioned on mask, and evaluated on the real test split. They were incrementally added to the training process while keeping the size of the real train split constant.

Scaling the augmentation set progressively improves the classification and segmentation performance of the training data, as shown in Fig. 6, with the 3x and 2.5x augmented synthetic datasets outperforming the relatively smaller ones on all metrics. After 2.5x, the performance metrics plateau. These results demonstrate that PathDiff effectively contributes valuable synthetic data in every augmented set, consistently improving model performance across all downstream tasks as the size of the synthetic set increases, highlighting PathDiff generates diverse high-quality data for histopathology image analysis.

### 7. Qualitative Comparison of Synthetic Images

In this section, we present a qualitative comparison of synthesized images generated by PathDiff, DiffMix [34], SDM [47], and ControlNet [50].

#### 7.1. Mask-to-Image examples

Fig. 7 shows a comparison of synthetic images generated on the PanNuke [12], CoNIC [15], and MoNuSAC [46] datasets. As illustrated in the figure, images generated by DiffMix appear very coarse with additional artifacts and fail to preserve the accurate stain colors observed in the original images. Consistent with observations reported by [31], we find that SDM-generated images display unrealistic color overlay artifacts. The color distribution of ControlNet-generated images appears highly inconsistent, being significantly inaccurate in some cases while better than others in certain instances. On the other hand, PathDiff accurately follows the cell mask and maintains the cell stain colors as seen in the original images.

#### 7.2. Text-to-Image examples

Fig. 9 shows samples generated by PathDiff and ControlNet. As with images conditioned on masks, ControlNet fails to preserve details in the original image and exhibits impractical colors uncommon in histopathology images. This explains the high FID and KID values compared to PathDiff in Tab.3

of the main paper.

### 7.3. Unified Paired Conditions Sampling

Fig. 8 shows images generated from paired Text and silver standard masks. PathDiff generated images incorporated guidance from both Text and Mask successfully and look significantly better than ControlNet.

### 8. Domain Expert Assessment

We acknowledge that traditional fidelity metrics like FID [17] are only somewhat applicable to histological images as large image datasets like ImageNet [5] would unlikely have images from this specific domain. Therefore, we conduct expert evaluation to validate the efficiency of the generated samples. We surveyed two domain experts—a physician and a pathology researcher—to review the generated data and assess if the samples accurately reflect the characteristics of real specimens.

**Image Preference Experiment:** We presented domain experts with a total of 200 synthetic images (Quadruplets of 50) generated from PathDiff, SDM [47], ControlNet [50], DiffMix [34]. Each Quadruplet of images was generated using the same conditional mask. Domain experts were asked to choose one of the four images that looked most real. As shown in Fig. 10, both domain experts preferred PathDiff-generated images significantly more than the existing SOTA methods, indicating our generated images look more realistic to an expert eye compared to others.

Actual Label	Predicted Label	
	Real	Synthetic
Synthetic	15	12
Real	11	16

Table 6. Confusion matrix for a domain expert distinguishing Real vs. Synthetic images.

**Expert Turing Test:** In this experiment, a domain expert (physician) was presented with a total of 54 samples in equal numbers of real and synthetic images in random order. Real labels of images are hidden. We ask to choose whether the given image looks

Tab. 6 shows domain expert’s performance in distinguishing real from synthetic images. Out of 27 synthetic images, 12 were correctly identified, while 15 were mistaken as real. Among 27 real images, 11 were correctly labeled, with 16



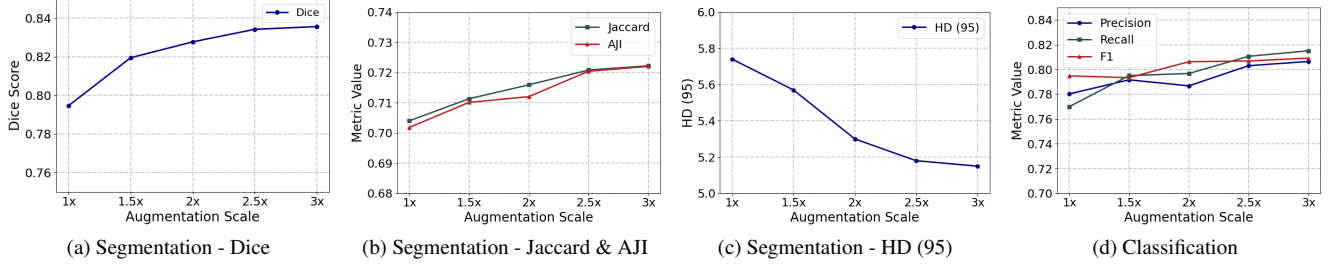


Figure 6. **Comparison of segmentation and classification metrics on the PanNuke [12] dataset across augmentation scaling factors.** The addition of PathDiff-generated synthetic data consistently increases downstream classification and segmentation performance. 1x uses one *synthetic* augmentation set equal to the *real* train split size; 1.5x adds another *synthetic* set equal to 1.5 times the *real* train split size and so on. After 2.5x, the performance metrics plateau.

### Algorithm 2 Unified Conditional Sampling

---

**Require:**  $\omega$ : guidance strength  
**Define**  $\mathbf{c} \in \{(\emptyset_{\mathbf{m}}, \mathbf{c}_t), (\mathbf{c}_m, \emptyset_t), (\mathbf{c}_m, \mathbf{c}_t)\}$   
 $\{1, \dots, T\}$ : timesteps with decreasing noise schedule  $\alpha = \{\alpha_t\}_{t=1}^T$   
1: **Initialize:**  $\mathbf{z}_T \sim \mathcal{N}(\mathbf{0}, \mathbf{I})$   
2: **for**  $t = T$  **to** 1 **do**  
3:   ▷ Form classifier-free guided score at timestep  $t$   
 $\tilde{\epsilon}_\theta(\mathbf{z}_t, \mathbf{t}, \mathbf{c}) = (\mathbf{1} + \omega)\epsilon_\theta(\mathbf{z}_t, \mathbf{t}, \mathbf{c}) - \omega\epsilon_\theta(\mathbf{z}_t, \mathbf{t})$   
4:   ▷ Denoise step to obtain intermediate sample  $\tilde{\mathbf{z}}_t$   
 $\tilde{\mathbf{z}}_t = \frac{\mathbf{z}_t - \sqrt{1 - \alpha_t} \tilde{\epsilon}_\theta(\mathbf{z}_t, \mathbf{t}, \mathbf{c})}{\sqrt{\alpha_t}}$   
5:   **if**  $t > 1$  **then**  
6:     **Sample**  $\mathbf{z}_{t-1} \sim \mathcal{N}(\mu_\theta(\mathbf{z}_t, \tilde{\mathbf{z}}_t, \mathbf{t}), \Sigma_\theta(\mathbf{z}_t, \mathbf{t}))$   
7:   **else**  
8:      $\mathbf{z}_0 = \tilde{\mathbf{z}}_t$   
9:   **end if**  
10: **end for**  
11: **return**  $\mathbf{z}_0$

---

falsely classified as synthetic. The overall accuracy was approximately 42.6. This indicates the user found it somewhat challenging to differentiate real from synthetic images. *real* or *synthetic*.

## 9. Sampling Algorithm

We use classifier-free guidance to sample from conditional and unconditional diffusion models to update the final score. Algorithm 2 gives overview of the sampling. We either randomly pair the conditions from non-overlapping M2I and T2I datasets or generate silver standard masks for T2I dataset (or can generate caption/relevant text condition for M2I dataset).

## 10. Considerations for $p_{split}$

When training jointly on two datasets—Text-to-Image and Mask-to-Image— $p_{split}$  controls the proportion of data sampled from each of them. We evaluate performance with three values of  $p_{split}$ : 0.2, 0.5, and 0.8. Results using only text are shown in Table 7, mask-only conditioning in Tab. 8, and both text and mask conditioning in Tab. 9.

In these experiments,  $p_{split} = 0.5$  strikes a balance, explaining why we chose this value in the main paper. While it seems logical to assign a larger probability to the larger dataset to cover more of its samples, we found that  $p_{split} = 0.5$  works well in practice, ensuring samples from both datasets are included at least once per epoch.

$p_{split}$	PathCap: Train			PathCap: Test		
	FID ↓	KID ↓	PLIP ↑	FID ↓	KID ↓	PLIP ↑
$p_{split} = 0.2$	16.33	0.0624	24.43	15.74	0.0603	24.50
$p_{split} = 0.5$	18.52	0.0619	24.18	19.60	0.0644	24.05
$p_{split} = 0.8$	19.58	0.0649	24.34	18.87	0.0626	24.27

Table 7. **Considerations for  $p_{split}$ .** CLIP-FID [17, 39], KID [2], and PLIP [21] similarity scores for different  $p_{split}$  values on PathCap [43], with text condition  $c_t$  used for sampling. PLIP [21] similarity scores on the real PathCap train and test splits are **26.34** and **26.56**, respectively, provided as a reference for comparison.

$p_{split}$	PanNuke: Train		PanNuke: Test	
	FID ↓	KID ↓	FID ↓	KID ↓
$p_{split} = 0.2$	7.36	0.0525	7.88	0.0559
$p_{split} = 0.5$	6.94	0.0389	7.28	0.0415
$p_{split} = 0.8$	8.57	0.0584	8.97	0.0707

Table 8. **Considerations for  $p_{split}$ .** CLIP-FID [17, 39], KID [2] for different  $p_{split}$  values on PanNuke [12] dataset. Only mask condition  $c_m$  was used for sampling.

## 11. In-Domain FID Results

For a more faithful assessment of pathology image quality, we compute an in-domain FID using the CONCH [29] encoder rather than relying solely on CLIP or Inception-based features, which were trained on general natural images and may not capture the nuances of histopathology. CONCH [29] is a foundation model trained on large pathology image-text pairs.

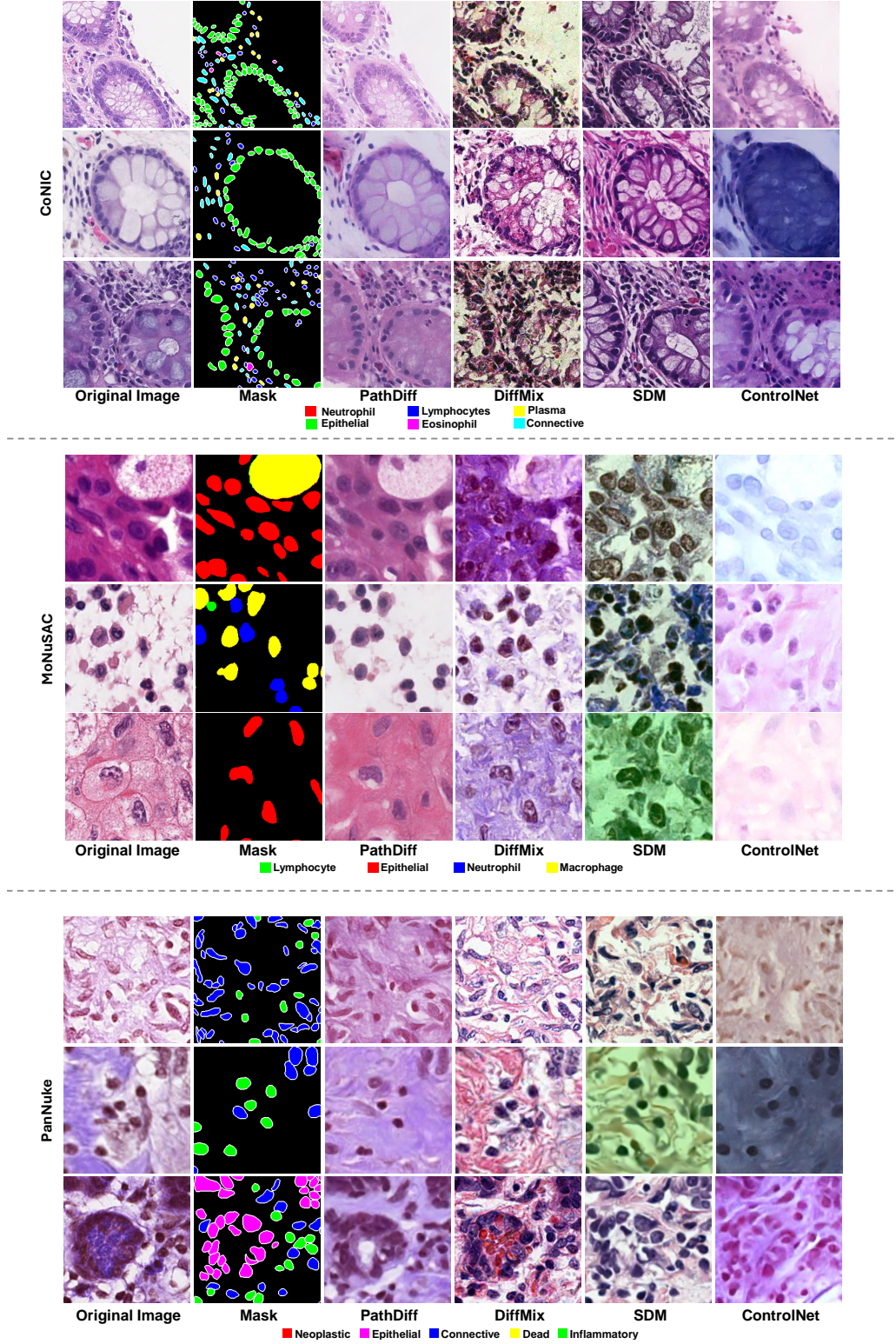


Figure 7. **Qualitative comparison** of synthetic images generated by PathDiff, DiffMix [34], SDM [47], and ControlNet [50] on the CoNIC [15], MoNuSAC [46], and PanNuke [12] datasets.



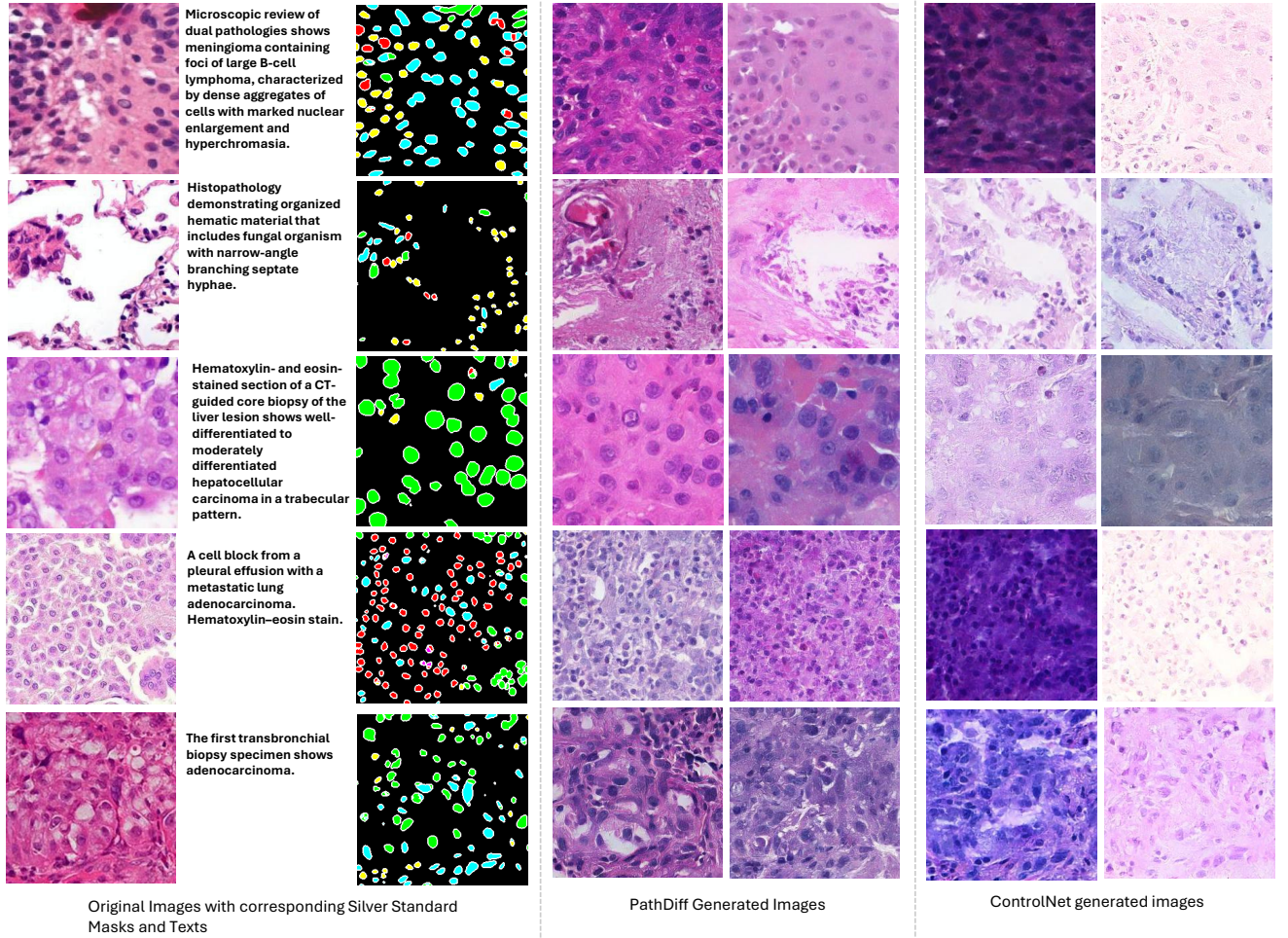


Figure 8. Qualitative comparison of Pathdiff and ControlNet generated images on paired Silver standard masks and texts.

$p_{split}$	PanNuke				PathCap					
	Train		Test		Train			Test		
	FID ↓	KID ↓	FID ↓	KID ↓	FID ↓	KID ↓	PLIP ↑	FID ↓	KID ↓	PLIP ↑
$p_{split} = 0.2$	10.25	0.0672	11.99	0.0800	15.21	0.0846	23.01	16.07	0.0956	22.81
$p_{split} = 0.5$	11.03	0.0718	12.32	0.0952	14.39	0.0884	23.01	14.26	0.1059	22.80
$p_{split} = 0.8$	9.723	0.0729	10.37	0.0862	12.78	0.0955	22.97	12.53	0.1107	22.70

Table 9. **Consideration for  $p_{split}$ .** CLIP-FID [17, 39], KID [17], and PLIP [21] similarity scores for different  $p_{split}$  values for PanNuke [12] and PathCap [43]. We used both text  $c_t$  and mask  $c_m$  for sampling.

## 12. Mask Depth Ablation

We test the effect of using two types of conditioning mask, first cell type mask and other is instance mask. We generate mask edges from instance mask using image processing technics. Using both masks generates better quality images as seen in Tab. 12, subsequently we use the mask depth of 6.

We simply increase the channel size of the Mask embedder  $M$  and concatenate two masks as input.

## 13. Choice of Pretrained Checkpoints

We tried different pretrained checkpoints choices in three module components: VAE, Text-Encoder, and Unet.

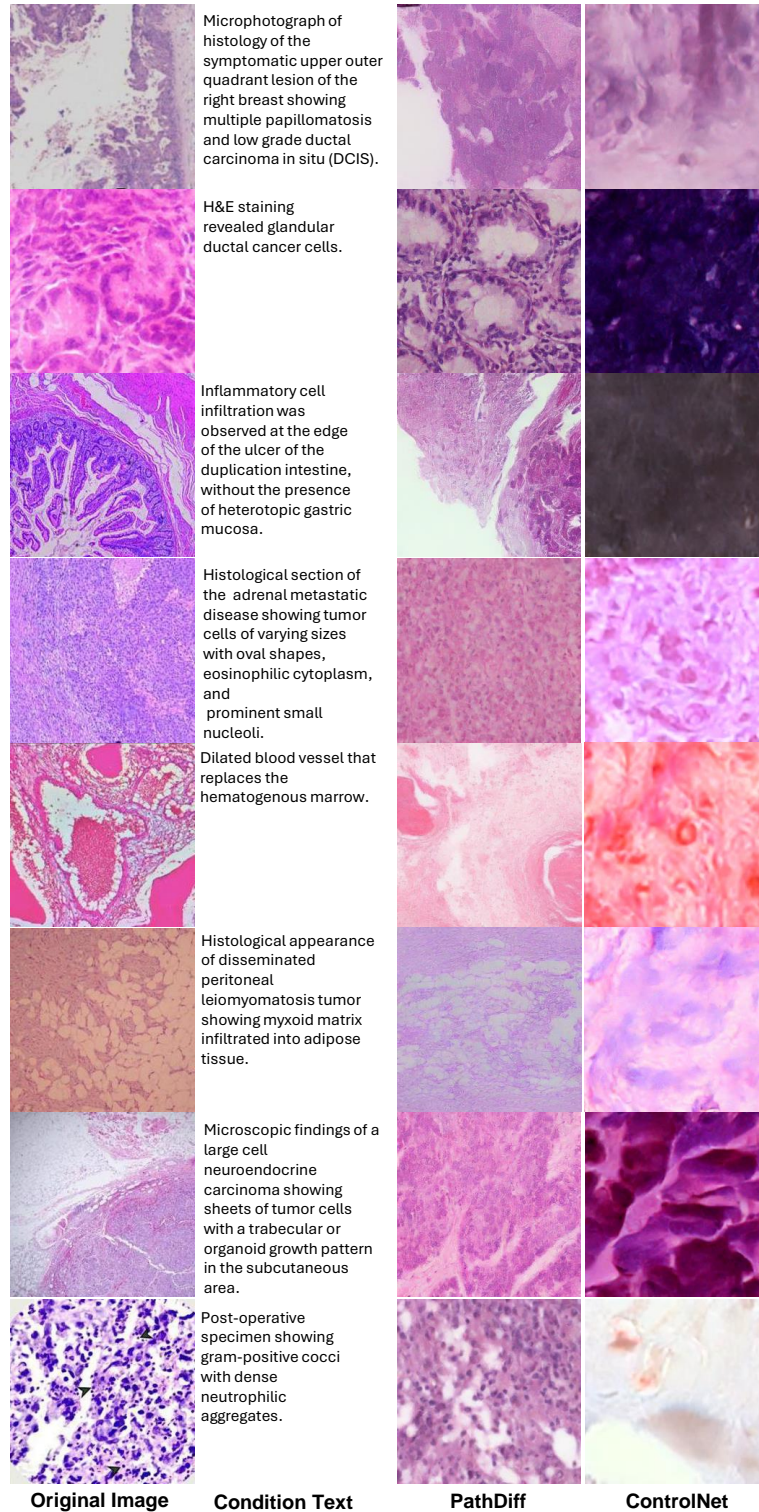


Figure 9. **Qualitative comparison** of synthetic images generated by PathDiff and ControlNet [50] on the PathCap [43] dataset.



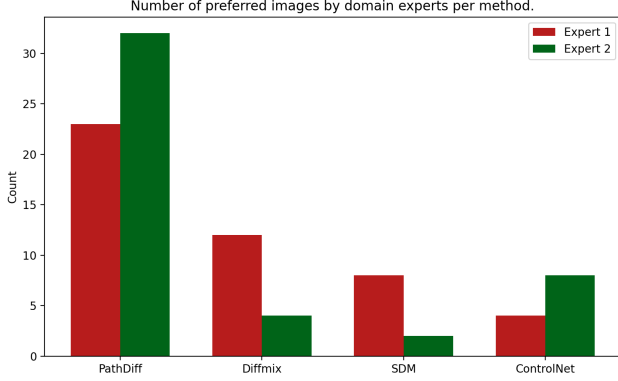


Figure 10. Both domain experts significantly preferred PathDiff generated images over other methods.

Method	PanNuke	CoNIC	MoNuSAC
Diffmix	119.35	257.92	290.27
SDM	177.30	<u>143.48</u>	<u>166.65</u>
ControlNet	<u>121.57</u>	174.74	277.96
PathDiff	<b>53.74</b>	<b>91.21</b>	<b>121.61</b>

Table 10. **Comparison of CONCH-FID** across training splits for PanNuke [12], CoNIC [15], and MoNuSAC [46]. PathDiff is trained jointly with T2I dataset: PathCap [43]. ControlNet [50] uses SD [40] backbone trained on the PathCap dataset.

Method	PanNuke	CoNIC	MoNuSAC
ControlNet	347.77	343.39	331.61
PathDiff	<b>153.77</b>	<b>156.21</b>	<b>141.88</b>

Table 11. **Comparison of CONCH-FID** on training splits for T2I dataset: PathCap. PathDiff is jointly trained with three M2I datasets: PanNuke [12], CoNIC [15], and MoNuSAC [46].

# mask_depth	PanNuke Test			
	IP $\uparrow$	IR $\uparrow$	CONCH FID $\downarrow$	KID $\downarrow$
<b>3</b>	0.79	0.47	102.37	0.0644
<b>6</b>	0.72	0.77	7.21	0.0415

Table 12. **Mask depth ablation** on PanNuke test split

**Finetuning VAE** The reconstruction performance of VAEs [40, 48] plays a crucial role in the fidelity of generated images. Losses introduced during the compression and decompression stages in VAEs compound with the denoising process losses in subsequent stages, directly impacting the quality of the generated images.

Initially, we used the VQ-VAE from [48], which was trained on the TCGA-BRCA [9] dataset containing whole-slide images (WSIs) exclusively from breast tissues. While

this VAE outperforms the one from [40], which was trained on natural images, its applicability is limited as it lacks representation of diverse tissue types. We fine-tuned the VAE on the datasets used in this work, including PanNuke [12], PathCap [43], CoNIC [15], and MoNuSAC [46].

As demonstrated in Tab. 13, fine-tuning the VAE on these datasets results in improvements across all reconstruction and generation metrics. However, these improvements, while consistent, are relatively modest.

VAE Trained on	Metrics			
	LPIPS $\downarrow$	SSIM $\uparrow$	MSE $\downarrow$	FID $\downarrow$
<b>TCGA-BRCA [9]</b>	0.0462	0.7962	0.0084	6.94
<b>Datasets: D</b>	0.0429	0.8212	0.0070	6.31

Table 13. **Effect of fine-tuning VAE on datasets D:** PanNuke [12], PathCap [43], MoNuSAC [46], and CoNIC [15].

**Text Encoder** To evaluate text–image alignment on the PathCap training set, we compared the similarity between each image and its corresponding report using two embedding methods. The CLIP-based similarity score was 21.56, while the PLIP-based score reached 26.30; clearly demonstrating that PLIP embeddings achieve stronger alignment between images and text. Therefore we used PLIP text encoder checkpoint in our experiments.

**Denoising U-net** We fine-tune the U-Net on the PathCap text-to-image dataset starting from the TCGA-BRCA checkpoint provided by [16]. The results are summarized in Tab. 14. We see improved CLIP-FID and KID scores for mask-to-image generation on PanNuke, as well as a higher PLIP similarity score for text-to-image generation on PathCap.

U-Net Checkpoint	CLIP FID $\downarrow$	PLIP Score $\uparrow$	KID $\downarrow$
<b>TCGA-BRCA</b>	14.44	21.79	0.1284
<b>PathCap</b>	7.21	24.05	0.0410

Table 14. **Comparison of U-Net checkpoints** on CLIP FID, PLIP score, and KID

## 14. Significance Test on Downstream Task:

We validate that PathDiff’s higher downstream scores aren’t due to chance by running a paired permutation test. We randomly swap method labels within each test example and compare mean F1/Dice across 1000 trials. The resulting p-values are  $< 0.05$  confirming PathDiff’s gains are statistically significant as seen in Fig. 11.

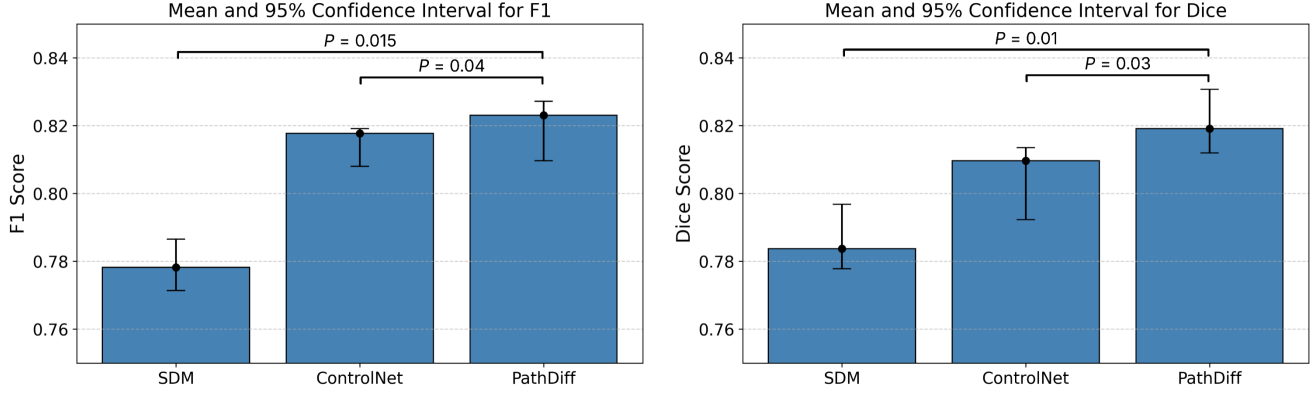


Figure 11. **Pairwise significance test**,  $p < 0.05$  indicates that PathDiff augmentation set helps improve downstream classification and segmentation tasks statistically significantly as compared to other methods.

## 15. Generation Performance on Hard Pathology Cases

To assess how well PathDiff handles challenging, clinically significant images, we split our test set into “pathological” (reports mentioning “carcinoma”) and “non-pathological” cases (reports describing benign findings). Table 15 compares FID, KID, and PLIP scores for each group. Although overall image fidelity remains similar, lower PLIP score for pathological cases suggest that images with malignant features are marginally more difficult to synthesize than benign ones.

Table 15. Performance on pathological vs. non-pathological cases

Case Type	FID ↓	KID ↓	PLIP ↑
Pathological	19.97	0.04	23.15
Non-pathological	20.10	0.06	24.13

## 16. Details on training previous works:

Diffmix and SDM are trained on M2I datasets only. We use their official repositories to refer to their code. For both DiffMix and SDM we use same training settings for all M2I datasets that of PanNuke [12] in [34]. For ControlNet we pre-trained SD[40] model on T2I data first and then used only M2I data for finetuning, as recommended in the official controlnet tutorial.

## 17. Computational Costs:

Since PathDiff only trains Unet encoder and shallow mask embedder, training costs remain modest, even for joint training. PathDiff trains 694 M parameters. Training time for the largest dataset combination (PathCap [43] + PanNuke [12]) is 30 Hours on 4 NVIDIA A6000 GPUs. Sam-

pling 6,300(train split of PanNuke) images takes 3.5-4.5 hours.

## 18. Survey Tool:

We used an interactive web-based tool to conduct a domain experts survey. Clear instructions were given to evaluate the images. Fig. 12 and Fig. 13 show the web interface used for the domain expert image preference experiment and the Turing test respectively.

### Image preference experiment

Thank you for considering taking part in this survey. The goal of this survey is to compare the quality of synthetic images on "Realism". Given the choice of images generated from different image generation methods which images would you prefer? Note that for each question same mask containing cell type was used to generate these images, therefore spatial structural similarity may be observed between samples.

1. Select an image that looks the most "real" to you.

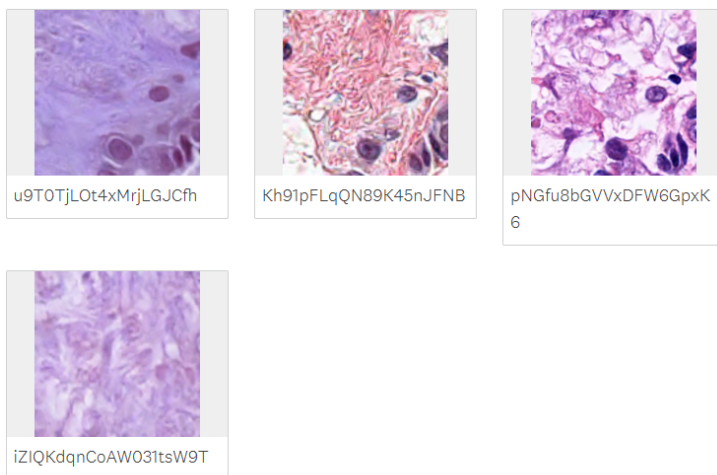
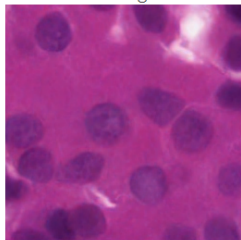


Figure 12. Interactive web interface used for domain expert image preference experiment.

### Turing Test

The goal of this part of the survey is to determine how well synthetically generated histopathology images can be visually discriminated from real-life samples by domain experts like you. You will be given an image choose whether you think it's "real" or "synthetic"?

51. Does this image look real or synthetic?



- ☐ Real
- ☐ Synthetic

52. Does this image look real or synthetic?

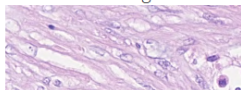


Figure 13. Interactive web interface used for domain expert Turing test.